Thermal fatigue as the origin of regolith on small asteroids

Marco Delbo[1], Guy Libourel[2,3], Justin Wilkerson[4], Naomi Murdoch[1,5], Patrick Michel[1], K. T. Ramesh[4], Clément Ganino[3], Chrystele Verati[3] & Simone Marchi[6]

Space missions[1,2] and thermal infrared observations[3] have shown that small asteroids (kilometre-sized or smaller) are covered by a layer of centimetre-sized or smaller particles, which constitute the regolith. Regolith generation has traditionally been attributed to the fall back of impact ejecta and by the break-up of boulders by micrometeoroid impact[4,5]. Laboratory experiments[6] and impact models[4], however, show that crater ejecta velocities are typically greater than several tens of centimetres per second, which corresponds to the gravitational escape velocity of kilometre-sized asteroids. Therefore, impact debris cannot be the main source of regolith on small asteroids[4]. Here we report that thermal fatigue[7–9], a mechanism of rock weathering and fragmentation with no subsequent ejection, is the dominant process governing regolith generation on small asteroids. We find that thermal fragmentation induced by the diurnal temperature variations breaks up rocks larger than a few centimetres more quickly than do micrometeoroid impacts. Because thermal fragmentation is independent of asteroid size, this process can also contribute to regolith production on larger asteroids. Production of fresh regolith originating in thermal fatigue fragmentation may be an important process for the rejuvenation of the surfaces of near-Earth asteroids, and may explain the observed lack of low-perihelion, carbonaceous, near-Earth asteroids[10].

The collisional and gravitational re-accumulation processes by which small asteroids are formed probably result in the creation of surfaces composed of boulders[11]. These boulders are broken up by micrometeoroid impacts into the smaller particles constituting the regolith[4,5]. A standard model[12] that calculates the time required to form regolith by fragmenting rocks of sizes between 1 and 10 cm by micrometeoroid impacts shows that these rocks on the Moon's surface will be broken down into smaller rocks in several million years[5,12]. Using the known[13] orbital distribution of micrometeoroids and a method[14] to calculate the impact probability of micrometeoroids with the Moon and asteroids (Methods), we find that the breakdown of surface rocks requires about the same amount of time on near-Earth asteroids (NEAs; asteroids with a perihelion distance of $q < 1.3$ AU, where 1 AU is the Earth–Sun distance) and on the Moon, whereas on main-belt asteroids (MBAs) this time is about ten times longer than on the Moon (Fig. 1).

Boulders on the surfaces of asteroids are also exposed to cyclic diurnal temperature variations, which cause mechanical stresses. To answer the question of whether these stresses are large enough to induce thermal

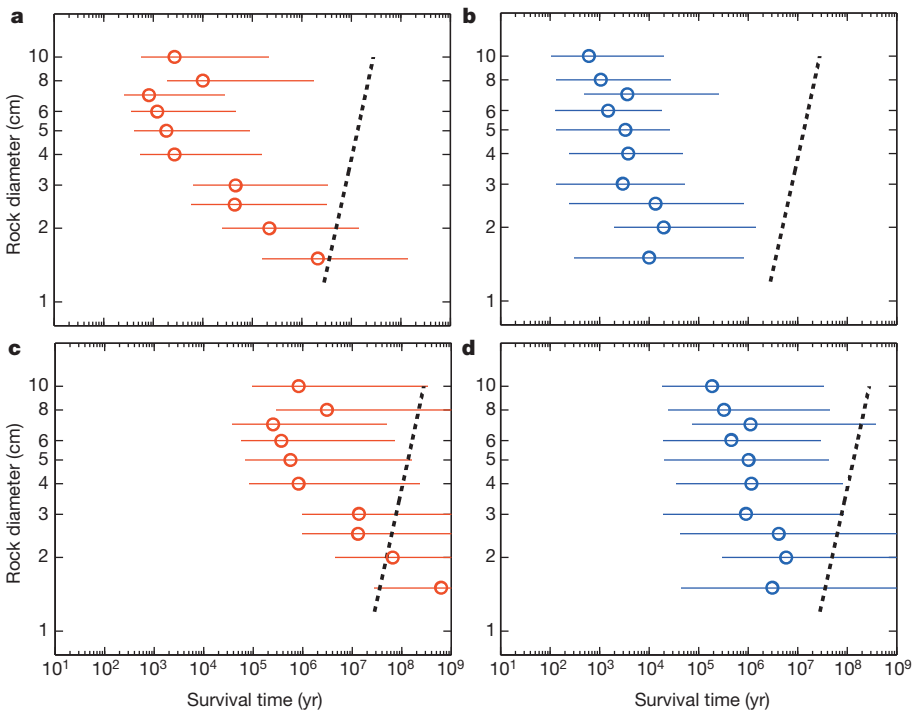

Figure 1 | Time required to break rocks on asteroids. Symbols show the time required to thermally fragment 90% of rocks for the nominal values of the model parameters. The thick dashed lines show the times at which 90% of these same rocks are broken by micrometeoroid impacts. **a**, Ordinary chondrite-like asteroid 1 AU from the Sun; **b**, carbonaceous chondrite-like asteroid at 1 AU; **c**, ordinary chondrite-like asteroid at 2.5 AU; **d**, carbonaceous chondrite-like asteroid at 2.5 AU. Error bars show the change in the thermal fragmentation time when model parameters are varied within their uncertainties (Methods).

[1]Laboratoire Lagrange, UNS-CNRS, Observatoire de la Côte d'Azur, Boulevard de l'Observatoire-CS 34229, 06304 Nice Cedex 4, France. [2]Université de Lorraine, CRPG-CNRS, 15 Rue Notre-Dame des Pauvres, BP 20, 54501 Vandoeuvre les Nancy, France. [3]Laboratoire Géoazur, UNS-CNRS, Observatoire de la Côte d'Azur, 250 rue Albert Einstein, Les Lucioles 1, Sophia-Antipolis, 06560 Valbonne, France. [4]Hopkins Extreme Materials Institute, Johns Hopkins University, Latrobe 122, 3400 North Charles Street, Baltimore, Maryland 21218, USA. [5]Institut Supérieur de l'Aéronautique et de l'Espace, 10 avenue Edouard-Belin, BP 54032, 31055 Toulouse Cedex 4, France. [6]Solar System Exploration Research Virtual Institute, Institute for the Science of Exploration Targets, Southwest Research Institute, 1050 Walnut Street, Suite 300 Boulder, Colorado 80302, USA.

fatigue crack growth, we perform laboratory experiments (Methods) on two meteorites: a carbonaceous chondrite (CM2 Murchison) and an ordinary chondrite (L/LL3.2 Sahara 97210) considered the closest available analogues of the broad asteroid spectroscopic classes C and S, respectively. Our protocol (Extended Data Fig. 1) consists of using a climatic chamber to subject these meteorites to temperature cycles that approximate the day–night temperature variations experienced on NEA surfaces. The temperature cycle period was taken to be 2.2 h, the fastest period permitted by our climatic chamber, allowing us to have a reasonable number of cycles within a month (still subjecting meteorites to temperature rates of change typical of NEA surfaces). The magnitude of the temperature excursion, ΔT, was taken to be 190 K, equal of the ΔT of C-type NEAs at ~0.7 AU from the Sun (Methods and Extended Data Fig. 2).

After subjecting the meteorites to as few as 407 temperature cycles, we use X-ray tomography to observe (Fig. 2) and measure (Methods) an increase in the length and in the width of several of the pre-existing cracks in both Murchison and Sahara 97210, thus confirming thermal fatigue (measurements for 21 cracks for each meteorite are shown in Extended Data Figs 3 and 4). Additionally, we found particles in the sample holder of Murchison that had broken off from its surface as a result of temperature cycling (Fig. 3). Crack growth and fragmentation due to either the manipulation of the samples or the freeze–thaw of water are both ruled out (Methods and Extended Data Fig. 5).

A second question is how much time is required for pre-existing cracks to propagate enough to break the rocks and contribute to the generation of finer regolith. Our measurements show that, under laboratory conditions, pre-existing cracks are extending in length at a rate of about 0.5 mm yr^{-1} (average of Murchison and Sahara 97210). A constant crack propagation rate would suggest that a 1-cm rock on the surface of an NEA could fragment into smaller pieces in less than 20 yr, several orders of magnitude faster than comminution by micrometeoroid impacts, which requires about 2 Myr on NEAs and about 20 Myr on MBAs. However, the crack propagation rate is typically a nonlinear function of crack size, thus requiring a detailed fracture mechanics analysis to investigate whether such a rapid growth rate would be maintained to the point of fragmentation and whether thermal fragmentation can also occur for different cycle periods, for larger rocks and at lower temperatures (for example for MBAs).

To investigate this question, we develop a micromechanical model (Methods) based on well-established thermal diffusion[15], thermo-mechanical[16] (Extended Data Fig. 6) and fracture mechanics[17] models in order to analyse the progressive crack growth from the early stages to final fragmentation (model parameter values are in Extended Data Table 1).

First we compare the crack growth measured in our laboratory experiments with model predictions. We use thermal boundary conditions simulating those of the laboratory experiments: the entire surface of a

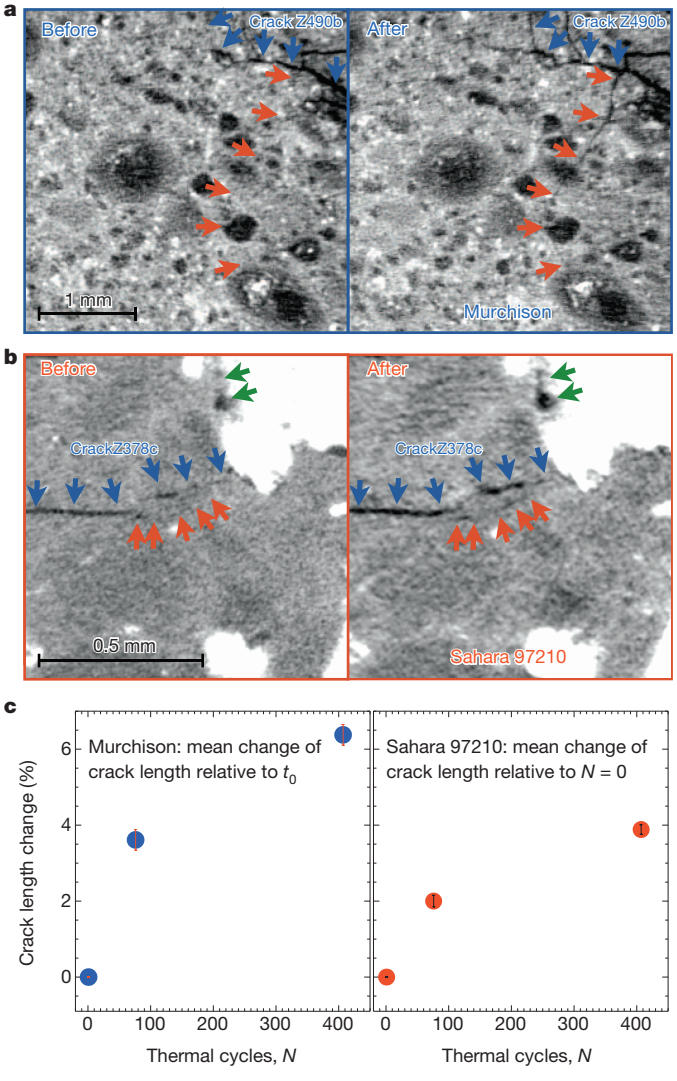

Figure 2 | Crack growth in meteorites due to laboratory temperature cycling. Arrows of the same colour mark growing cracks in the pictures before and after temperature cycling. **a**, Murchison; **b**, Sahara 97210. The cracks volume and length growth are given in the Extended Data Figs 3 and 4, respectively. **c**, The mean change of the length of the 21 measured cracks for each meteorite as a function of the number of thermal cycles. Statistical errors are 1σ.

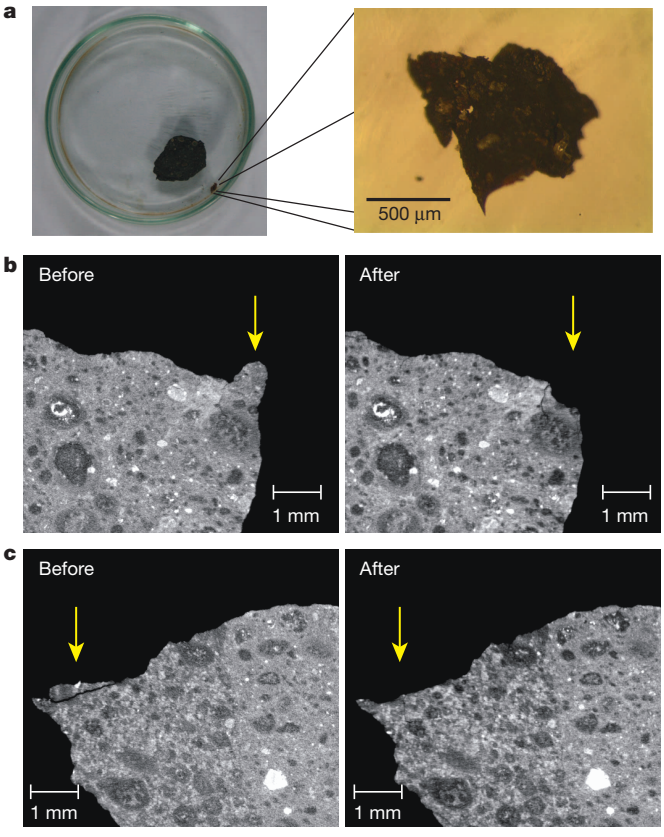

Figure 3 | Regolith formation from Murchison in the laboratory. **a**, The sample of Murchison and (enlarged) one of its small fragments, containing several visible chondrules, found in the sample holder after temperature cycling. **b**, **c**, Tomographic slices of regions of the same sample of Murchison before and after temperature cycling. The arrows indicate fragments that broke off from Murchison.

rock 1 cm in diameter is forced to follow sinusoidal temperature oscillations with $\Delta T = 190$ K and a period of 2.2 h. Considering the idealized nature of the model, the agreement with the experimental measurements is satisfactory (the average model-to-experiment discrepancy is 20%; see Methods and Extended Data Fig. 7) and indicates that we have captured the essential aspects of thermal fatigue crack growth.

Next we use the model to provide predictions for the time (number of day–night temperature cycles) required to achieve thermal fragmentation for surface rocks with sizes between 1 and 10 cm (Extended Data Fig. 8) on C- and S-type asteroids at 1 and 2.5 AU from the Sun. Here the cycle period is taken to be 6 h, which is more appropriate than 2.2 h for most small asteroids. The day–night temperature variations, temperature gradients and mechanical stresses are calculated using boundary conditions appropriate for asteroid surfaces radiatively heated by the Sun (Methods). We use a conservative definition of rock fragmentation in our model, namely that an initial 30-μm-long crack grows to a length equal to the rock diameter. Shorter cracks can still produce fragments, either by merging with other growing cracks or by a flaking mechanism (as in the case of Fig. 3).

Our results (Fig. 1) demonstrate that, at 1 AU from the Sun, centimetre-sized rocks fragment on asteroids at least an order of magnitude faster by thermal fragmentation than by comminution by micrometeoroid impacts, the previously assumed dominant mechanism. We also find (Fig. 1) that although larger rocks require more time to fragment by micrometeoroid impact, the trend is reversed for thermal fragmentation. Therefore, thermal fragmentation of a 10-cm rock is predicted to occur orders of magnitude faster than fragmentation due to micrometeoroid impact. Although the speed of thermal fatigue is reduced at larger heliocentric distances (Extended Data Fig. 2), we still find (Fig. 1) that in the main belt, 2.5 AU from the Sun, thermal fatigue fragmentation is, in general, and within the errors of our model (Methods and Extended Data Fig. 9), more quickly than rock break-up by micrometeoroid impacts.

Because regolith formation by thermal fragmentation does not depend on asteroid size, this process occurs also on larger asteroids (for example, those varying in size from several tens to several hundreds of kilometres).

We argue that asteroid rock thermal fragmentation has observable implications: by breaking down rocks into smaller pieces and thus exposing new surface area, thermal fragmentation can provide a mechanism to make fresh regolith. Because the process of thermal fragmentation is strongly dependent on the value of ΔT, the rate of thermal fragmentation increases with decreasing perihelion distance (Extended Data Fig. 2). Observations show that the fraction of NEAs with fresh surfaces, whose reflectance spectra resemble those of ordinary chondrites ('Q-type' asteroids), is increasing with decreasing perihelion distance with a dependence[18] that mimics the curves of the NEA ΔT. From this result, a concrete, testable prediction is that more regolith should be found on NEAs that, during their chaotic dynamical evolution, are likely to have spent more time with smaller perihelion distances[19].

We also predict that small NEAs (for example those 100 m in radius) with low perihelion distances ($q < 0.3$ AU) could be eroded by thermal fragmentation and radiation pressure sweeping[20] on timescales shorter than their dynamical lifetime. For instance, at 0.3 AU the solar radiation pressure can remove grains with radii of the order of millimetres from the surface of an asteroid with a radius of 100 m (ref. 20); these grains can be produced by thermal fragmentation of centimetre-sized rocks in less than ~200 yr. Therefore, low-perihelion NEAs loose regolith at a rate of roughly 5×10^{-5} m yr^{-1}, implying that an object with a radius of 100 m would be completely eroded in about 2 Myr. Because thermal fragmentation is faster for C-type NEAs than for S-type NEAs (Fig. 1), we predict that erosion would be faster for carbonaceous NEAs, providing an explanation for the shortage of low-albedo, carbonaceous Aten-type NEAs[10].

METHODS SUMMARY

Rock comminution by micrometeoroid impacts on asteroids. We calculate the impact probability of micrometeoroids of the zodiacal dust cloud[13] on the Moon, on a typical NEA and on MBAs using the method of ref. 14 but without imposing any impact velocity cut-off. The ratio of the rock survival times on NEAs and MBAs to the known lunar value[12] is proportional to the respective impact probability ratios.

Thermal fatigue laboratory experiments. We perform two sets of temperature cycles (respectively 76 and 331, for a total of 407) on centimetre-sized samples of the meteorites Murchison (CM2) and Sahara 97210 (L/LL3.2). Before and after the first set of cycles, and after the second set, meteorites are imaged using a computed tomographic scanner. The scanned volumes are aligned and the increases in volume and length of several (21) cracks are measured.

Thermomechanical and fatigue crack growth model. Asteroid rock (Extended Data Fig. 8) temperatures are calculated for heliocentric distances between 0.3 and 2.5 AU. We use a well-established one-dimensional thermal model[15]. Model parameters are as follows[21]: rotational period, 6 h; thermal inertia, $\Gamma = 640$ J m^{-2} s$^{-0.5}$ K^{-1} (carbonaceous chondrite) or $\Gamma = 1{,}800$ J m^{-2} s$^{-0.5}$ K^{-1} (ordinary chondrite); bolometric albedo, $A = 0.02$ (carbonaceous) or $A = 0.1$ (ordinary). The cyclic spatial and temporal temperature fields are used to calculate the strains and stresses in the rocks and the stress intensity factors at the tip of surface cracks that, following Paris's law[17], grow downwards through the rocks in the direction perpendicular to the asteroid surface. The time needed to propagate a crack from 30 μm to a length equal to the rock diameter is then compared with the rock survival time against micrometeoroid impact (Fig. 1).

Online Content Any additional Methods, Extended Data display items and Source Data are available in the online version of the paper; references unique to these sections appear only in the online paper.

Received 28 June 2013; accepted 11 February 2014.
Published online 2 April 2014.

1. Veverka, J. *et al.* The landing of the NEAR-Shoemaker spacecraft on asteroid 433 Eros. *Nature* **413,** 390–393 (2001).
2. Yano, H. *et al.* Touchdown of the Hayabusa spacecraft at the Muses Sea on Itokawa. *Science* **312,** 1350–1353 (2006).
3. Gundlach, B. & Blum, J. A new method to determine the grain size of planetary regolith. *Icarus* **223,** 479–492 (2013).
4. Housen, K. R., Wilkening, L. L., Chapman, C. R. & Greenberg, R. Asteroidal regoliths. *Icarus* **39,** 317–351 (1979).
5. Hörz, F. & Cintala, M. Impact experiments related to the evolution of planetary regoliths. *Meteorit. Planet. Sci.* **32,** 179–209 (1997).
6. Housen, K. R. & Holsapple, K. A. Ejecta from impact craters. *Icarus* **211,** 856–875 (2011).
7. McFadden, L., Eppes, M., Gillespie, A. & Hallet, B. Physical weathering in arid landscapes due to diurnal variation in the direction of solar heating. *Geol. Soc. Am. Bull.* **117,** 161–173 (2005).
8. Luque, A., Ruiz-Agudo, E., Cultrone, G., Sebastián, E. & Siegesmund, S. Direct observation of microcrack development in marble caused by thermal weathering. *Environ. Earth Sci.* **62,** 1375–1386 (2011).
9. Viles, H. *et al.* Simulating weathering of basalt on mars and earth by thermal cycling. *Geophys. Res. Lett.* **37,** L18201 (2010).
10. Mainzer, A. *et al.* Characterizing subpopulations within the near-earth objects with NEOWISE: preliminary results. *Astrophys. J.* **752,** 110–126 (2012).
11. Michel, P. & Richardson, D. C. Collision and gravitational reaccumulation: possible formation mechanism of the asteroid Itokawa. *Astron. Astrophys.* **554,** L1 (2013).
12. Hoerz, F., Schneider, E., Gault, D. E., Hartung, J. B. & Brownlee, D. E. Catastrophic rupture of lunar rocks: a Monte Carlo simulation. *Moon* **13,** 235–258 (1975).
13. Nesvorný, D. *et al.* Cometary origin of the zodiacal cloud and carbonaceous micrometeorites. implications for hot debris disks. *Astrophys. J.* **713,** 816–836 (2010).
14. Briani, G., Morbidelli, A., Gounelle, M. & Nesvorný, D. Evidence for an asteroid-comet continuum from simulations of carbonaceous microxenolith dynamical evolution. *Meteorit. Planet. Sci.* **46,** 1863–1877 (2011).
15. Spencer, J. R., Lebofsky, L. A. & Sykes, M. V. Systematic biases in radiometric diameter determinations. *Icarus* **78,** 337–354 (1989).
16. Čapek, D. & Vokrouhlický, D. Thermal stresses in small meteoroids. *Astron. Astrophys.* **519,** A75 (2010).
17. Janssen, M., Zuidema, J. & Wanhill, R. *Fracture Mechanics* 2nd edn, 207–213 (Spon, 2004).
18. Marchi, S., Magrin, S., Nesvorný, D., Paolicchi, P. & Lazzarin, M. A spectral slope versus perihelion distance correlation for planet-crossing asteroids. *Mon. Not. R. Astron. Soc. Lett.* **368,** L39–L42 (2006).
19. Marchi, S., Delbo, M., Morbidelli, A., Paolicchi, P. & Lazzarin, M. Heating of near-Earth objects and meteoroids due to close approaches to the sun. *Mon. Not. R. Astron. Soc.* **400,** 147–153 (2009).
20. Jewitt, D. The active asteroids. *Astron. J.* **143,** 66–80 (2012).
21. Opeil, C. P., Consolmagno, G. J. & Britt, D. T. The thermal conductivity of meteorites: new measurements and analysis. *Icarus* **208,** 449–454 (2010).

Acknowledgements This work was supported by the French Agence National de la Recherche (ANR) SHOCKS, the BQR of the Observatoire de la Côte d'Azur (OCA), the University of Nice-Sophia Antipolis, the Laboratory GeoAzur and the French National

Program of Planetology (PNP). We benefited from discussions with K. J. Walsh and W. F. Bottke. A. Morbidelli helped with the dynamical model. M. Moumni, J.-M. Hiver and G. Thomas helped with the experiments, X-ray tomography and early data analysis. G.L. conducted part of his work as an INSU-CNRS delegate. S.M. acknowledges support from NASA SSERVI. The comments of S. Byrne improved this work fundamentally. Computations and data analysis were done on the CRIMSON cluster at OCA.

Author Contributions M.D. and S.M. inspired the laboratory experiments, which were designed by G.L., C.G., P.M., C.V. and M.D. Experiments were carried out by G.L. N.M. and M.D. developed the methods of crack volume and length measurement. N.M. and M.D. applied the methods to the experimental data. J.W., K.T.R. and M.D. worked on the thermomechanical model that was mostly developed and used by J.W. The scientific analysis was directed by M.D. with frequent discussions with G.L., P.M., J.W., K.T.R. and C.G. Computer codes were developed by M.D., J.W. and N.M. M.D., J.W., G.L., P.M., N.M., K.T.R. and C.G. jointly drafted the manuscript, with all authors reviewing it and contributing to its final form.

Author Information Reprints and permissions information is available at www.nature.com/reprints. The authors declare no competing financial interests. Readers are welcome to comment on the online version of the paper. Correspondence and requests for materials should be addressed to M.D. (delbo@oca.eu) or G.L. (libou@oca.eu).

METHODS

Rock comminution by micrometeoroid impacts on asteroids. On asteroids, like on the Moon, regolith formation via break-up of rocks by micrometeoroid impacts is accomplished by two mechanisms: rupture and erosion[5]. On the Moon, rock survival time against micrometeoroid rupture is in the range between 2 and 20 Myr for rock diameters between 1 and 10 cm (ref. 12). This survival time on asteroids can be calculated by the following method.

First, given the relation between the rock diameter and the meteoroid impact energy required for the rock rupture[12], and assuming densities of 1 g cm^{-3} for cometary meteorids and 3.5 g cm^{-3} for asteroidal meteoroids, one can find that rocks 1–10 cm in size are broken up by sub-millimetre meteoroids[5]. Meteoroids of this size dominate the zodiacal dust cloud[13,14], 90% of which is constituted by cometary dust[13].

Next, given the orbital distribution of these cometary particles[13], we use a classical method[14], but without imposing an impact velocity cut-off, to calculate the average intrinsic impact probabilities (p, for example, the number of impacts per meteoroid on a circular cross-section of radius 1 km per year) and the average impact velocity (v_i) of meteoroids on the Moon, a typical NEA ($a = 1$ AU, $e = 0.3$, $i = 0.15$ rad; where a is the semimajor axis of the orbit, e is its eccentricity and i is its inclination) and an average MBA. We find that $p = 8.0 \times 10^{-18}$ and $v_i = 11$ km s^{-1} for the Moon, that $p = 9.5 \times 10^{-18}$ and $v_i = 15$ km s^{-1} for a typical NEA, and that $p \approx 1 \times 10^{-18}$ and $v_i = 10$ km s^{-1} for an average MBA. Neglecting the different impact velocities (because the energy for rock break-up, E_b, is a shallow function of the impact velocity[12]: $E_b \propto v_i^{0.7}$), the rate of meteoroid impacts per unit time and unit surface, Φ, on the Moon, NEAs and MBAs is proportional to p. We thus have $\Phi_{NEA} \approx \Phi_{Moon} \approx 10\Phi_{MBA}$.

Hence, the rock survival time on NEAs is similar to that on the Moon (we assume that they are the same in Fig. 1), whereas on MBAs rocks survive about ten times longer. For rocks in the size range 1–10 cm, erosion removes surface material at a rate of order 1 mm Myr^{-1} (refs 5,12), requiring at least ~10–100 Myr to comminute rocks on the Moon and on NEAs, and 0.1–1 Gyr on MBAs.

Thermal fatigue laboratory experiments. Our experimental protocol is presented in Extended Data Fig. 1. To 'image' the cracks in the meteorites at three stages of thermal fatigue (before the temperature cycles, t_0; after 76 cycles, t_1; and after 407 cycles, t_2), we use a Phoenix Nanotom computed tomography scanner that produces three-dimensional data cubes of approximately 1,000^3 voxels or 2,000^3 voxels depending on the spatial resolution, $\Delta\lambda$. Specifically, for Murchison $\Delta\lambda = 12.5$, 13, 13 μm, and for Sahara 97210 $\Delta\lambda = 3.75$, 4, 4.5 μm, at t_0, t_1 and t_2, respectively. The higher spatial resolution for Sahara 97210 is necessary because this meteorite has fewer and thinner cracks than Murchison. The orientation of each sample within the scanned volume varies between t_0, t_1 and t_2. Because the determination of crack growth requires the comparison of sizes of same cracks at t_0, t_1 and t_2, we precisely align and scale the meteorites within the computed tomography scans. To do this, several distinctive features in the meteorites, such as metal-rich inclusions of a few voxels in volume, are visually identified at t_0, t_1 and t_2, and used as position markers. Because the objects are not initially aligned, the same marker does not necessarily have the same coordinates at t_0, t_1 and t_2. For each meteorite, we determine the matrices that best transform the marker coordinates at t_1 and at t_2 to those at t_0. A Monte Carlo method is used to calculate the best transformation matrix by minimizing the square of the distance between the marker coordinates at t_0 and the transformed ones. We then use the procedure TRANSFORM_VOLUME, written in IDL by Martin Downing, to apply the transformations to align the computed tomography volumes at t_1 and t_2 with those at t_0 (see www.idlcoyote.com/programs/transform_volume.pro; IDL is developed by Exelis Visual Information Solutions Incorporated (http://www.exelisvis.com/ProductsServices/IDL.aspx)). The accuracy of the final alignment is, in general, of the order of 1 voxel.

We develop a method for the determination of the volume and length of the cracks that is not sensitive to the absolute value of the voxel intensity. This is because the X-ray intensity is not constant between different computed tomography scans, causing variability of the meteorite voxel counts, the background counts and the noise level among scans of the same meteorite. We measure the crack width at all voxels along the crack length, and the crack height, within a volume of interest of the meteorite that includes the crack or a portion thereof. We use the same volume of interest for the same crack at t_0, t_1 and t_2 on the aligned computed tomography scans. The volume of interest, different for each different crack, is defined as follows. We chose a plane (for example, the x–y plane) along which the crack mainly extends, and we extract several slices from the computed tomography volume parallel to the considered plane. Typically, we consider ten slices. For each slice, we draw a segmented line that follows the crack as closely as possible; the same number of segments is used for each slice. For each segment and for each slice, we determine the width of the crack and the width uncertainty in the direction perpendicular to the segment at every point. We calculate the volume of the crack portion from

$$V = \sum_{i=n}^{N} \sum_{j=1}^{M_i} \sum_{k=1}^{L_{i,j}} W_{i,j,k} g_{i,j,k} (\Delta\lambda)^3 \quad (1)$$

where $W_{i,j,k}$ is the crack width at the kth position along the jth segment of length $L_{i,j}$ on the ith slice of the volume of interest. The initial and final slices are n and N, respectively, and M is the number of segments. The value of $g_{i,j,k}$ is equal to 1 or 0 depending on whether the width determination was accepted or deemed invalid using the procedure described in the next paragraph. As for the width of the crack, we use the full-width at half-maximum of the Gaussian function that best fits the intensity profile of the meteorite perpendicular to the segment. We prefer to give the volume of the crack instead of its average width. This is because cracks typically have large width variations throughout their volume. The accuracy of the crack width determination is estimated at each point by a Monte Carlo method: we attempt to fit a Gaussian function up to 9,000 times to the meteorite intensity profile to have at least 30 valid fits. Gaussian random noise (with a standard deviation given by noise in the computed tomography data) is added to the voxel counts in each iteration. If at t_0, t_1 or t_2 the dispersions of the widths, centres or amplitudes of the Gaussian fits are larger than some threshold values that, once tuned, are kept constant for both meteorites at all times, the point is deemed not to contain a crack and is excluded from the sums of equation (1) at t_0, t_1 and t_2 (by setting the corresponding value of g to zero).

The crack length measurement method is similar to the one used for the crack volume determination, but with two main differences. First we select a volume of interest that includes one or more crack tips, typically by constructing the segments such that they partly extend beyond the crack tips. This is because any potential increase in the length of the crack due to temperature cycling must happen at the crack tip. Next, for each slice, we count the number of voxels where $g = 1$, that is, where a valid crack width is found. We note that, contrary to the method used for the measurement of the crack volume, we do not set $g = 0$ at t_0, t_1 and t_2 if $g = 0$ at t_0, t_1 or t_2. We observe that our method fails to fit a Gaussian function to the meteorite intensity profile beyond the crack tip and that the dispersions of the Gaussian parameters can become very large, indicating the absence of a crack. The length of the crack averaged over the slices of interest is given by

$$L = \frac{1}{N-n} \sum_{i=n}^{N} \sum_{j=1}^{M_i} \sum_{k=1}^{L_{i,j}} g_{i,j,k} \Delta\lambda$$

We take the standard error of the mean as the error in the length of the crack. This same process is applied to the computed tomography scans of the meteorites at t_0, t_1 and t_2 to measure the evolution of crack length as a function of the number of the cycles.

We were concerned that processes other than thermal fatigue could affect crack growth in our experiments. For example, the water freeze–thaw effect has an important role in the opening of cracks in terrestrial rocks. Atmospheric moisture in the cracks of our specimens could, in principle, have been present and may have facilitated the opening and the lengthening of cracks. However, we rule out this mechanism in our experiments in two ways. First, temperature cycling of our samples is carried out under an anhydrous atmosphere at a pressure of 1 bar. Next, before the temperature cycling begin, the meteorite specimens are exposed to a vacuum of ~10^{-2} bar and later immersed in an argon–nitrogen gas for several hours to eliminate potential traces of humidity.

We were also concerned that the transport of the meteorites from the climatic chamber to the computed tomography scanner may have stressed the samples and affected the crack growth. We rule out this effect by obtaining scans of a sample of Murchison that was transported from the climatic chamber to the scanner, but not subjected to temperature cycles. We repeat this procedure twice. Visual inspection of the scan images shows no obvious change in the position, width and length of the cracks, and no formation of new cracks. Also, no fragments flaking off from the surface of the Murchison specimen were found (analysis of the scans shows no obvious change in the surface of the specimen). Volume measurements of several cracks in the specimen of Murchison that was transported but not subjected to temperature cycles show no variation within the error bars (Extended Data Fig. 5).

Thermomechanical and fatigue crack growth model. Our thermomechanical and crack growth model is based on the coupling of a well-established thermal diffusion model[15], linear elastic fracture mechanics and a well-established fatigue crack growth law (Paris's law[17]). Paris's law relates the rate at which the crack length, a, grows as a function of the number of cycles, N, to the maximum stress intensity factor[17] excursion, ΔK_I:

$$\frac{da}{dN} = C[\Delta K_I(a)]^n \quad (2)$$

where C and n are material properties fitted to experimental fatigue data[22].

First, we use a well-established thermal model[15] to solve the one-dimensional heat diffusion problem and calculate the temperature, $\bar{T}(x,t)$, as a function of time, t, and depth, x, in a layer of rocks of different sizes at the asteroid surface (Extended Data Fig. 8). We use the same boundary conditions and finite-difference implementation as in ref. 15, but we adopt a higher spatial resolution of 0.025 times the heat penetration depth[15], and a maximum depth is set at 1,024 resolution elements. We model a surface area at the equator. We set the initial temperatures to zero, and we let the model evolve until the mid-day temperature of the surface at the asteroid rotation $N+1$ is within 0.1 K of the temperature at the rotation N. The parameters that control the values of $\bar{T}(x,t)$ are the thermal inertia, Γ, the bolometric albedo, A, and the asteroid rotation period, P. We model two cases whose thermal parameters, taken from ref. 21, are $\Gamma = 640\ \mathrm{J\,m^{-2}\,s^{-0.5}\,K^{-1}}$, $A = 0.02$ and $\Gamma = 1{,}800\ \mathrm{J\,m^{-2}\,s^{-0.5}\,K^{-1}}$, $A = 0.1$, corresponding to those of carbonaceous and ordinary chondrites, respectively (Extended Data Table 1). We set $P = 6$ h, which is appropriate for small asteroids. The thermal model does not account for the rock boundaries, which increase the porosity of the medium, resulting in lower thermal inertia and probably increasing the thermal gradients.

To model the temperatures in the meteorites in our laboratory experiments, we modify the thermal model by solving the heat diffusion problem for an idealized spherical, homogeneous and isotropic body (with the thermal properties of a carbonaceous or an ordinary chondrite, as above) whose surface temperature is forced to follow a sinusoidal function in time with a period of 2.2 h and an amplitude of 190 K, independently of the mineralogy and equal to those imposed on the meteorites in the climatic chamber.

Next we compute the time-dependent macroscopic stress field, $\Sigma(x,t)$, associated with the transient thermal gradients following established methods[16]. Additionally, we account for the microscopic stress fields, $\sigma(x;y,t)$, that develop as a result of the heterogeneous microstructure of the material, assuming different thermal expansion coefficients for the matrix and the chondrules (the two main components of those meteorites). Finally, the maximum stress intensity excursion experienced over a temperature cycle is used in Paris's law to compute the growth rate of a planar crack originating from the surface of rock (a flow chart of the procedure is shown in Extended Data Fig. 6).

Consider a two-scale body (Extended Data Fig. 6) with two macroscale observable quantities, namely macroscopic stress, $\Sigma(x,t)$, and macroscopic temperature, $\bar{T}(x,t)$, which are functions of the macroscale material coordinate x. Likewise, the microscale quantities $\sigma(x;y,t)$ and $T(x;y,t)$ are functions of the microscale material coordinate y. The macroscale quantities are related to the microscale quantities through a suitable volumetric average, that is, $\Sigma(x,t) = v^{-1}\int_v \sigma(x;y,t)\,\mathrm{d}v$ and $\bar{T}(x,t) = v^{-1}\int_v T(x;y,t)\,\mathrm{d}v$. The microscale is heterogeneous, approximated by spherical inclusions embedded in a matrix. The linear thermoelastic properties of the inclusions are as follows: bulk modulus, K_i; shear modulus, μ_i; thermal expansion coefficient, α_i. Likewise, the linear thermoelastic properties of the matrix are K_m, μ_m and α_m. The macroscale is homogenized with effective linear thermoelastic properties of $\bar{K}$, $\bar{\mu}$ and $\bar{\alpha}$ (Extended Data Table 1).

The macroscopic stresses, $\Sigma(x,t)$, develop as a result of spatial gradients in the macroscopic transient temperature field, $\bar{T}(x,t)$. The formulation of our macroscopic stress field is very similar to that in ref. 16. We confirm that the macroscopic stress fields used in this study agree with finite-element analysis.

In general, additional microscale stresses in excess of the macroscale stresses are generated by both the heterogeneous microstructure, that is, $\alpha_\mathrm{i} \neq \alpha_\mathrm{m}$, as well as microscale gradients in the microscale temperature field, that is, $\nabla_y T(x;y,t)$. For simplicity, we assume that the microscale temperature field is equal to the macroscopic temperature field at a particular macroscale location, that is, $T(x;y,t) = \bar{T}(x,t)$, thus neglecting any microscopic gradients in the microscopic temperature field.

Let the spherical inclusions of radii r_c be located on a cubic lattice with lattice parameter 2ℓ. The microscopic stress tensor associated with the thermal mismatch, σ^TM, is defined such that $\sigma(x;y,t) = \Sigma(x,t) + \sigma^\mathrm{TM}(x;y,t)$ and is calculated through a self-consistent, two-phase composite spheres approach. The method approximates the periodic array of spherical inclusions as a two-phase spherical assemblage with appropriate boundary conditions[23]. This approach approximates the stress-field interactions between inclusions[23]. The thermoelastic constitutive relations for both the inner solid sphere and outer spherical shell are expressed as

$$\sigma^\mathrm{TM} = \begin{cases} \left(K_\mathrm{i} - \frac{2}{3}\mu_\mathrm{i}\right)(I:\varepsilon^\mathrm{TM})I \\ \quad + 2\mu_\mathrm{i}\varepsilon^\mathrm{TM} - 3K_\mathrm{i}\alpha_\mathrm{i}\Delta\bar{T}I & 0 \le \|y\| \le r_\mathrm{c} \\ \left(K_\mathrm{m} - \frac{2}{3}\mu_\mathrm{m}\right)(I:\varepsilon^\mathrm{TM})I \\ \quad + 2\mu_\mathrm{m}\varepsilon^\mathrm{TM} - 3K_\mathrm{m}\alpha_\mathrm{m}\Delta\bar{T}I & r_\mathrm{c} < \|y\| \le \ell \end{cases}$$

where tensorial notation is used, ε^TM is the total microscopic linear strain associated with the thermal mismatch, and I is the identity (where the tensor product $A:B$ is defined as $A_{ij}B_{ij}$).

The microscopic equilibrium equation yields the following solution for the microscopic hoop stresses associated with thermal mismatch:

$$\sigma^\mathrm{TM}_{\theta\theta}(x;y,t) = \begin{cases} K^\mathrm{TM}\Delta\alpha\Delta\bar{T}(x,t)(r_\mathrm{c}^3\ell^{-3} - 1) & 0 \le \|y\| \le r_\mathrm{c} \\ \frac{1}{2}K^\mathrm{TM}\Delta\alpha\Delta\bar{T}(x,t)(r_\mathrm{c}^3\|y\|^{-3} + r_\mathrm{c}^3\ell^{-3}) & r_\mathrm{c} < \|y\| \le \ell \end{cases}$$

where $\Delta\alpha = \alpha_\mathrm{i} - \alpha_\mathrm{m}$, $\Delta\bar{T}(x,t) = \bar{T}(x,t) - \bar{T}_0$, and K^TM is defined as

$$K^\mathrm{TM} = \frac{12\mu_\mathrm{m}K_\mathrm{i}K_\mathrm{m}}{3K_\mathrm{i}K_\mathrm{m} + 4\mu_\mathrm{m}K_\mathrm{m} + 4\mu_\mathrm{m}(K_\mathrm{i} - K_\mathrm{m})r_\mathrm{c}^3\ell^{-3}}$$

Returning to the body shown in Extended Data Fig. 6, we now consider the introduction of a planar crack originating from the surface of this body. On the macroscale the crack cuts through the diameter of the rock, and on the microscale the crack is assumed to cut through the array of chondrules. To perform the fatigue crack propagation analysis, it is necessary to obtain an expression for the stress intensity factor, K_I, which is dependent on both the loading and the geometry[17].

The stress intensity factor most closely associated with our geometry and loading conditions was obtained by ref. 24 as

$$K_\mathrm{I}(a,t) = \int_0^a \mathrm{d}\xi\ \frac{2e_\mathrm{n}^c \bullet \sigma(\xi,t)e_\mathrm{n}^c}{\sqrt{2\pi(a-\xi)}}\sum_{i=0}^{3} M_i\left(1 - \frac{\xi}{a}\right)^{i/2} \quad (3)$$

where σ is the total microscopic tensorial stress field that would develop along the crack plane if the crack were not present, e_n^c is the unit normal to the crack plane and M_i are geometric parameters that may be found in ref. 24. To make use of the transient stress intensity factor of equation (3) in the solution of equation (2), it is necessary to obtain the maximum stress intensity factor excursion, $\Delta K_\mathrm{I}(a)$, experienced over a particular cycle. Because we are dealing with thermal cyclic stress, the crack tip experiences both tensile and compressive stresses over a full cycle; therefore, ignoring crack closure[25], the lowest stress intensity factor that the crack tip experiences is simply zero. The resulting nonlinear ordinary differential equation—equation (2) after substitution of equation (3)—is solved numerically by an adaptive fourth-order Runge–Kutta method, providing the crack size as a function of the number of thermal cycles.

Lastly, we develop a method for providing some degree of model validation and uncertainty quantification. The chondrule size, r_c, and spacing, ℓ, are known with a high degree of accuracy because these are measured from our computed tomography scans. However, we expect a ~30% relative uncertainty in the values of the thermophysical parameters because their values were obtained through direct measurement of meteorites[16,26–30]. We thus calculate our model for several sets of values of the thermophysical parameters that we choose to within 30% of the nominal parameter values, and find an order-of-magnitude change in the predicted number of thermal cycles required to achieve rock fragmentation. This implies an order-of-magnitude change in the survival time of rocks in Fig. 1 and, therefore, that thermal fragmentation remains dominant over meteoroid impacts as a regolith generation mechanism.

To the best of our knowledge, no systematic fatigue crack growth experiments have been conducted on asteroid or meteorite materials. Therefore, we took the Paris's law parameters of Carrara marble[22], which satisfactorily predict the fatigue crack growth observed in our experiments (inset of Extended Data Fig. 7). Paris's law parameters dramatically different from those of Carrara marble will result in greater model–experiment discrepancy (Extended Data Fig. 9), which is defined as

$$\left|\frac{a_\mathrm{model}(N) - a_\mathrm{exp}(N)}{a_\mathrm{exp}(N) - a_\mathrm{exp}(N=0)}\right| \quad (4)$$

where a_model and a_exp are the crack lengths predicted by the model and those measured from our laboratory experiments, respectively. Even if the Paris's law exponent were 30% larger than the assumed value (Extended Data Fig. 9), the model would still predict that thermal fragmentation is the dominant regolith generation mechanism over comminution by micrometeroid impact.

22. Migliazza, M., Ferrero, A. & Spagnoli, A. Experimental investigation on crack propagation in Carrara marble subjected to cyclic loads. *Int. J. Rock Mech. Min. Sci.* **48,** 1038–1044 (2011).
23. Christensen, R. M. *Mechanics of Composite Materials* 31–58 (Krieger, 1979).
24. Glinka, G. & Shen, G. Universal features of weight functions for cracks in mode I. *Eng. Fract. Mech.* **40,** 1135–1146 (1991).
25. Suresh, S. *Fatigue of Materials* 2nd edn, 505–507 (Cambridge Univ. Press, 1998).

26. Medvedev, R. V., Gorbatsevich, F. I. & Zotkin, I. T. Determination of the physical properties of stony meteorites with application to the study of processes of their destruction. *Meteoritika* **44,** 105–110 (1985).
27. Flynn, G. J. Physical properties of meteorites and interplanetary dust particles: clues to the properties of the meteors and their parent bodies. *Earth Moon Planets* **95,** 361–374 (2004).
28. Hazen, R. M. Temperature, pressure and composition: structurally analogous variables. *Phys. Chem. Miner.* **1,** 83–94 (1977).
29. Anderson, O., Isaak, D. & Oda, H. Thermoelastic parameters for six minerals at high temperature. *J. Geophys. Res.* **96,** 18037–18046 (1991).
30. Smyth, J. R. High temperature crystal chemistry of fayalite. *Am. Mineral.* **60,** 1092–1097 (1975).

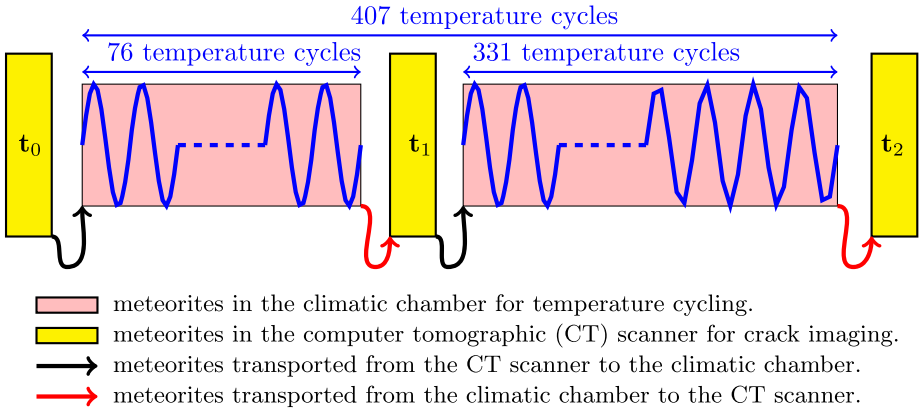

Extended Data Figure 1 | Protocol of the thermal fatigue laboratory experiments. We place samples of Murchison and Sahara 97210 ~1 cm in size in a climatic chamber where the air temperature is forced to follow cycles between 250 and 440 K with a period of 2.2 h. The air is anhydrous and at a pressure of 1 bar. Meteorites are analysed by X-ray computed tomography before the temperature cycles begin (t_0), after 76 cycles (t_1) and after 407 cycles (t_2). From the scans, we measure (Methods) the increases in the volume and length of cracks as functions of the number of temperature cycles.

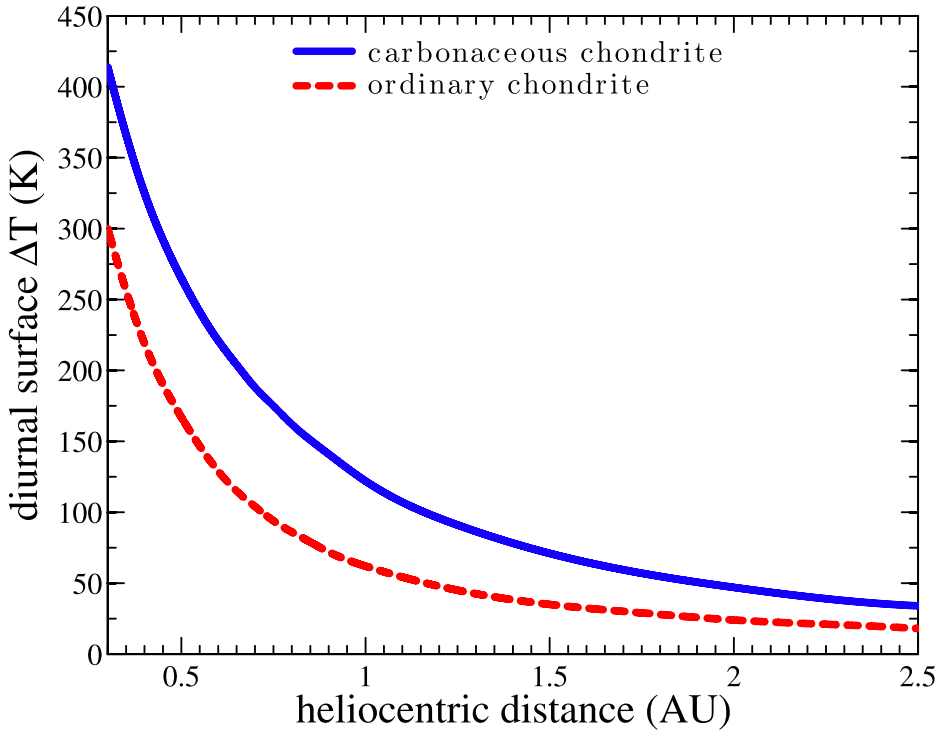

Extended Data Figure 2 | Diurnal surface temperature excursions on asteroids as a function of the distance to the Sun. Temperatures are calculated at the equator of a spherical asteroid by means of an asteroid thermophysical model[15] (Methods), assuming the thermal properties (Extended Data Table 1) of a carbonaceous chondrite (the CM2 Cold-Bokkevel) and that of an ordinary chondrite (the H5 Cronstad). The asteroid rotation period is set to 6 h. The bolometric albedo is assumed to equal 0.02 for the carbonaceous chondrite and 0.1 for the ordinary chondrite.

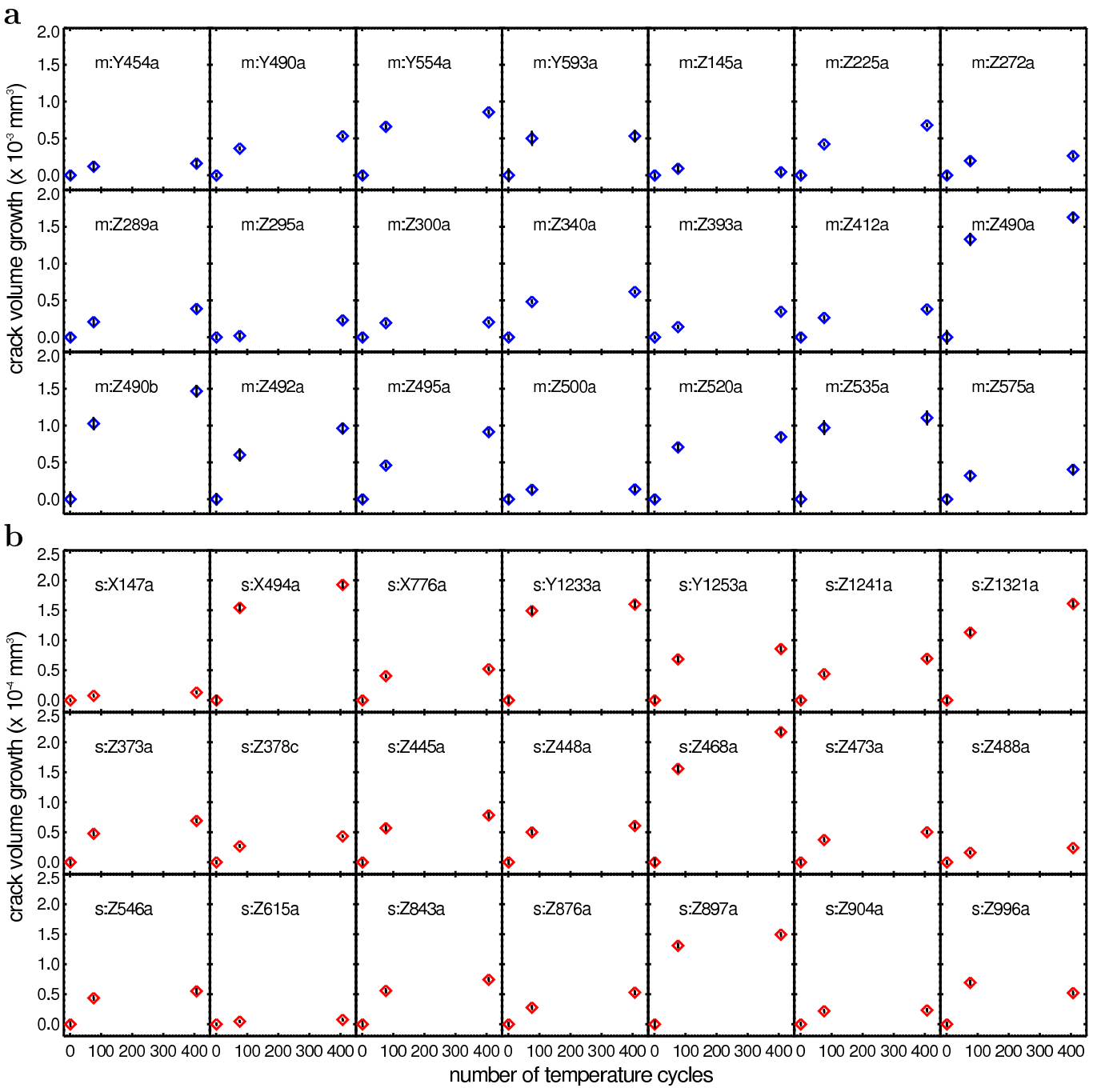

Extended Data Figure 3 | Volume growth of individual cracks as a function of the number of temperature cycles. **a**, Murchison; **b**, Sahara 97210. Statistical errors are 1σ and are in general smaller than the plot symbols. The crack volume is measured by the procedure described in Methods. Cracks are labelled with the value of the initial slice of the corresponding volume of interest. If different volumes of interest are defined with the same initial tomographic slice, the last letter of the crack label is used to identify the crack (for example Z387a, Z378b, Z378c).

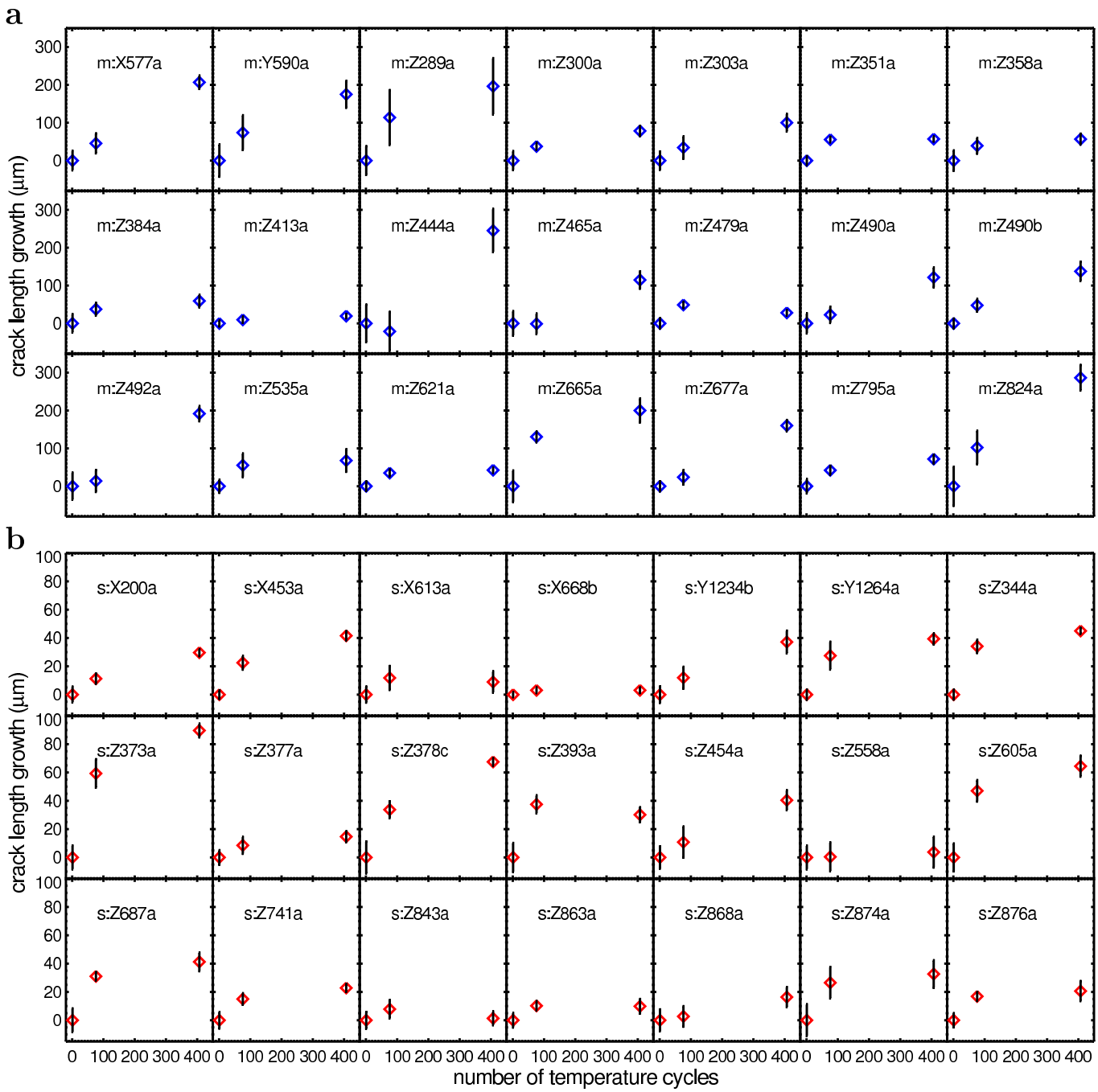

Extended Data Figure 4 | Length growth of individual cracks as a function of the number of temperature cycles. **a**, Murchison; **b**, Sahara 97210. Statistical errors are 1σ. The crack length is measured by the procedure described in Methods. See Extended Data Fig. 3 for crack labelling.

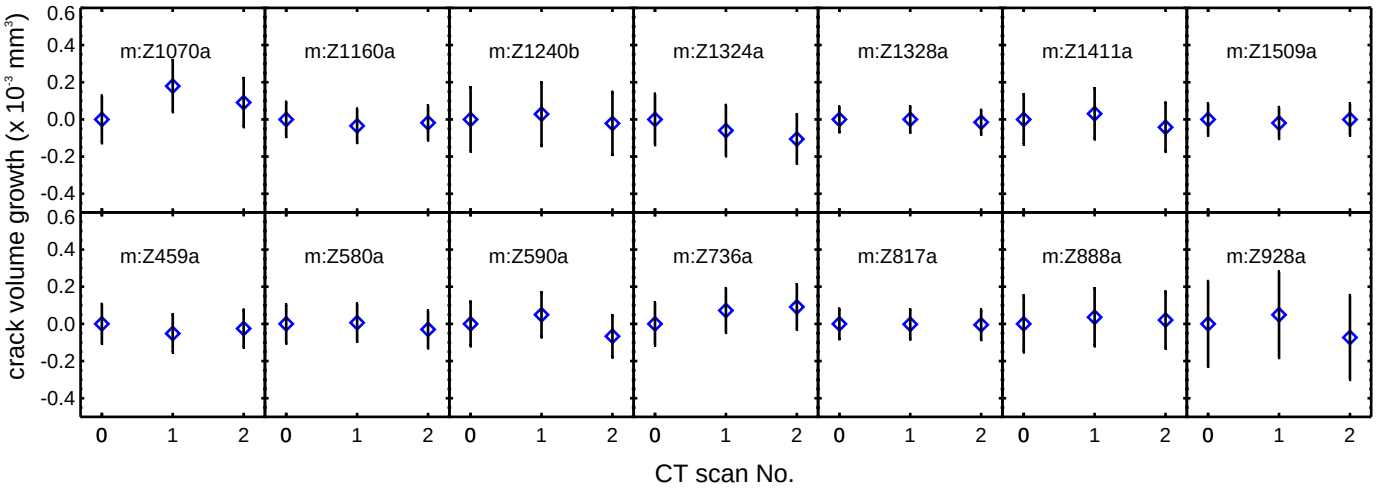

Extended Data Figure 5 | No crack growth with no temperature cycles. Volume growth of individual cracks in a specimen of Murchison that was transported from the climatic chamber to the computed tomography scanner without temperature cycling. Statistical errors are 1σ. The crack volume is measured by the procedure described in Methods. We performed three computed tomography scans: scan no. 0 (the label on the *x* axis) was obtained on the sample of the meteorite as it was received; scan no. 1 was carried out after the meteorite was transported from the computed tomography scanner to the climatic chamber and back; and scan no. 2 was obtained after a second transportation of the meteorite.

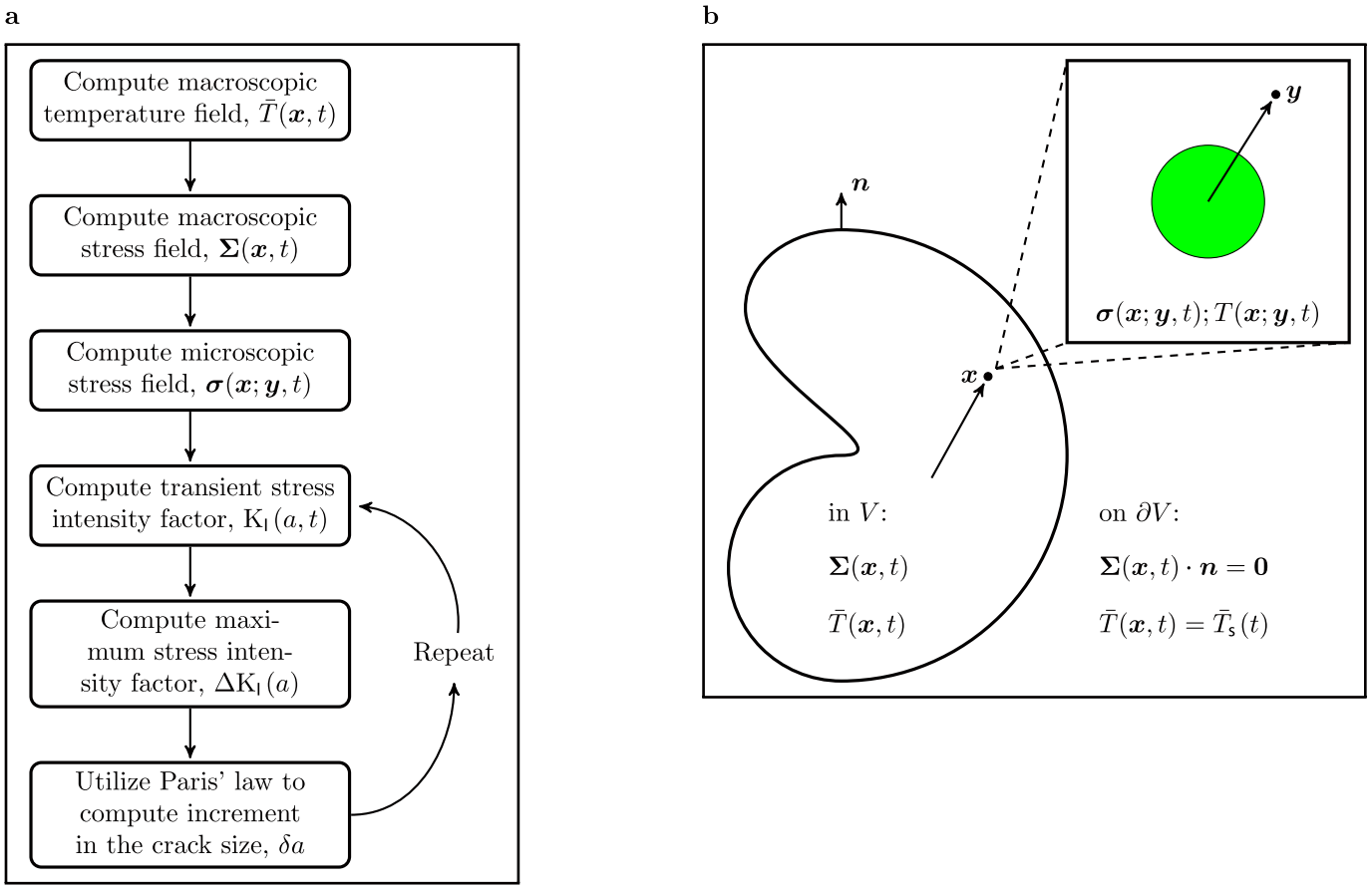

Extended Data Figure 6 | Schematics of our micromechanical model. **a**, Flow chart; **b**, schematic of the two-scale representation (Methods). ∂V is the surface of a body of volume V. A microscopic spherical inclusion, centred at the macroscopic point x is embedded in an infinite, effectively homogenized matrix. A general microscopic material point is located at a distance y measured from the centre of its nearest spherical inclusion located at x. The spherical inclusions of radius r_c are located at the vertices of a cubic lattice with lattice parameter 2ℓ.

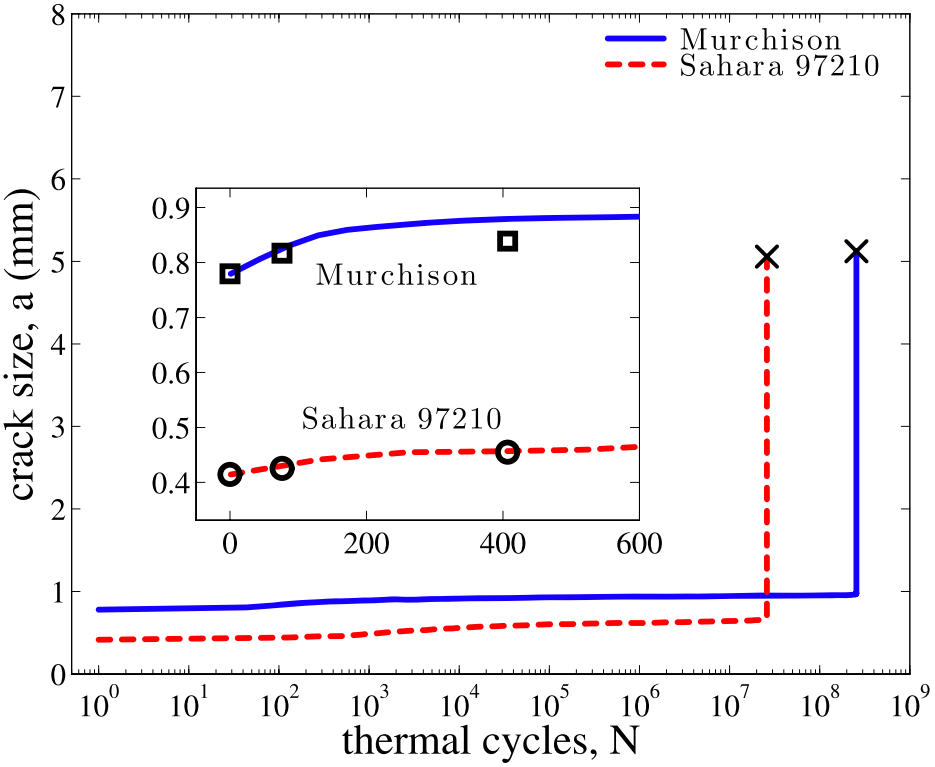

Extended Data Figure 7 | Comparison of theoretical and measured crack growth. Crack size is shown as a function of the number of temperature cycles predicted by our model and compared with experimental data for two particular cracks. Main plot: pre-existing cracks of 0.76 mm for Murchison and 0.41 mm for Sahara 97210 originating at the surface of the samples progressively propagate through the respective meteorites. The crosses indicate that the crack has reached a length equal to the meteorite diameter; therefore, full fragmentation occurs. Inset: comparison of the model with the length growth measured in our experiments for the same two cracks.

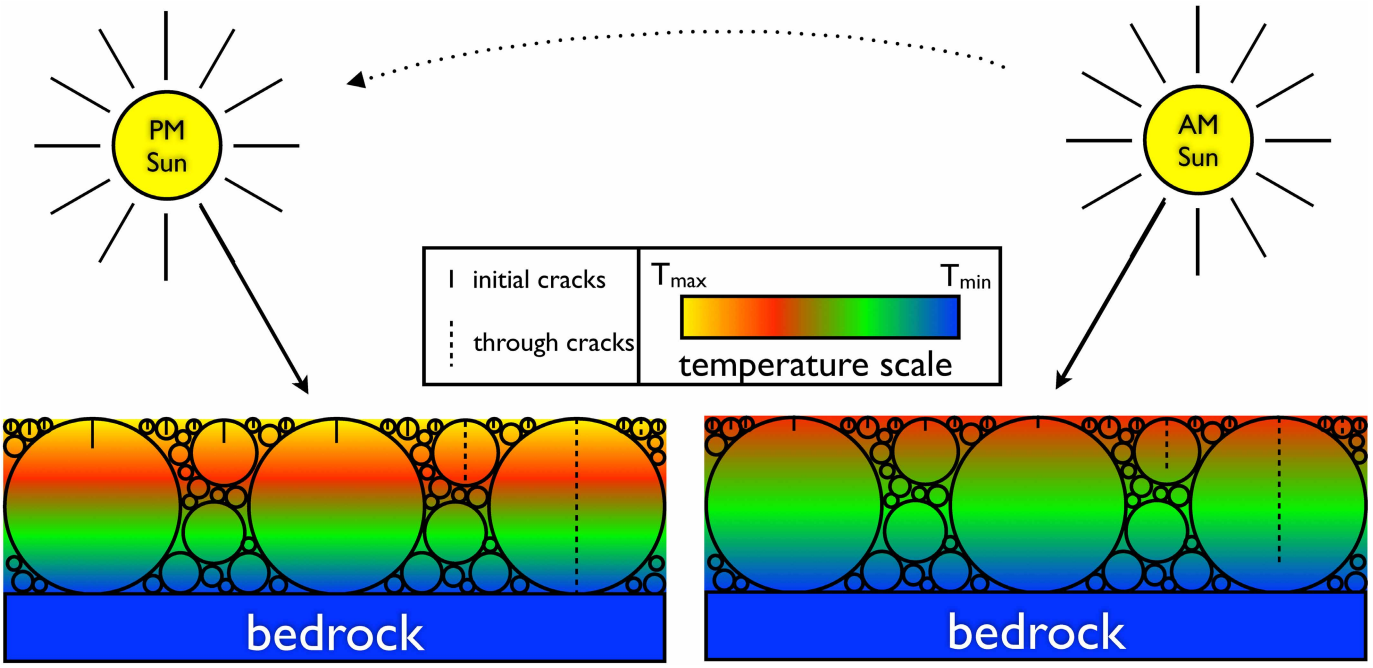

Extended Data Figure 8 | Schematic of the surface layer of rocks modelled in this work. The schematic is inspired by Fig. 3 of ref. 7. The layer is composed of rocks with different sizes. The rocks are subjected to spatial and temporal temperature gradients at the surface of the asteroid due to changes in the diurnal solar heating. The bottom of the rock layer is assumed to be in contact with bedrock that is deep enough to have a constant temperature. Temperatures are calculated assuming a uniform medium (no rock boundaries). This is probably a conservative approximation, because the presence of voids between rocks may enhance the temperature gradients owing to a reduction in the thermal conductivity. When the model starts, all rocks have a surface crack of the same length (30 μm), represented by the thin vertical line. It is very likely that cracks of this size, similar to the grain size of meteorites, are present in asteroidal material. Crack growth is from top to bottom. Crack growth is modelled until the time (survival time) the crack reaches the diameter of the rock (through-crack), and the rock is broken into two pieces. Rock survival times are shown in Fig. 1.

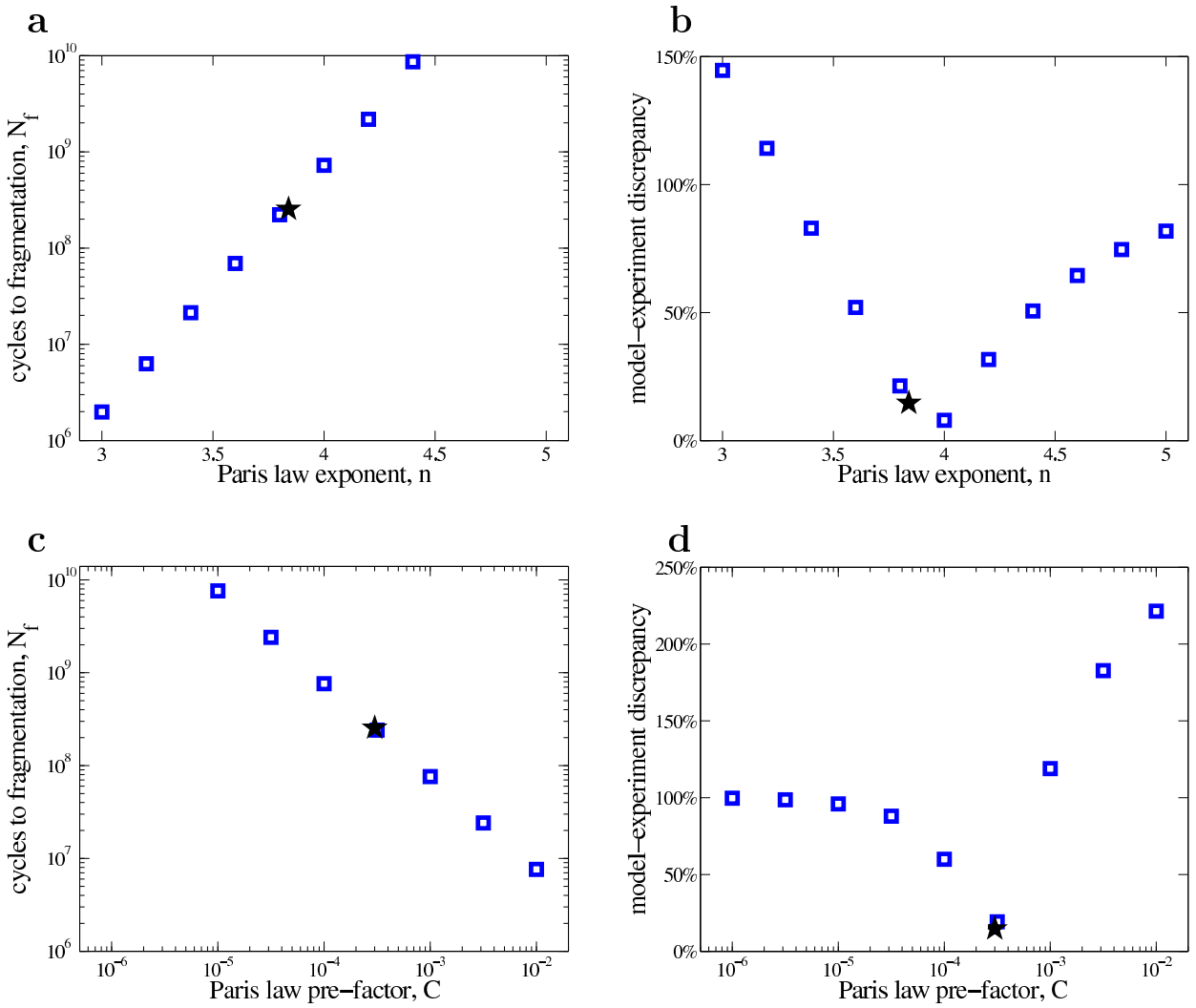

Extended Data Figure 9 | Sensitivity of the model results to variations in Paris's law parameters. The stars indicate model results for the nominal values of the parameters given in Extended Data Table 1. **a**, Number of temperature cycles until fragmentation for a rock 1 cm in diameter as a function of the Paris's law exponent, *n*. **b**, Discrepancy between the model and the experimental crack growth, defined by equation (4) in Methods, as a function of the Paris's law exponent. The model–experiment discrepancy is of the order of 20% for the nominal values of the *C* and *n*. A 100% discrepancy would be clearly visible in Extended Data Fig. 7. **c**, Same as **a**, but here the number of cycles until rock fragmentation is plotted as a function of the Paris's law factor *C*. **d**, Same as **b**, but here the discrepancy between the model and the experimental crack growth is plotted as a function of the Paris's law factor *C*.

Extended Data Table 1 | Physical properties of materials and their default values used in this work

	Units	Carbonaceous chondrite	Ordinary chondrite	Reference
Paris exponent, n		3.84	3.84	[23]
Paris pre-factor, C	$\mathrm{m\,[MPa\,\sqrt{m}]^{-n}}$	3×10^{-4}	3×10^{-4}	[23]
Bulk modulus, $\bar{K}$	GPa	29	56	[27, 26]
Chondrule modulus K_i	GPa	113	113	[28]
Shear modulus, $\bar{\mu}$	GPa	18	29	[27, 26]
Bulk expansion coefficient, $\bar{\alpha}$	$\mathrm{K^{-1}}$	8.5×10^{-6}	8.5×10^{-6}	[28]
Chondrule expansion coefficient, α_i	$\mathrm{K^{-1}}$	10.4×10^{-6}	10.4×10^{-6}	[30]
Thermal conductivity, κ	$\mathrm{W\,m^{-1}\,K^{-1}}$	0.5	1.88	[21]
Heat capacity, C	$\mathrm{J\,kg^{-1}\,K^{-1}}$	500	550	[21]
Bulk density, ρ	$\mathrm{kg\,m^{-3}}$	1662	3150	[21]
Average chondrule radius	mm	0.78	1.16	this work
Average chondrule spacing	mm	1.6	1.4	this work
Thermal inertia, Γ	$\mathrm{J\,m^{-2}\,s^{-0.5}\,K^{-1}}$	640	1800	[21]
Bolometric albedo, A		0.02	0.1	-
Asteroid rotation period, P	hours	6	6	-
Laboratory temperature cycle period, P	hours	2.2	2.2	-